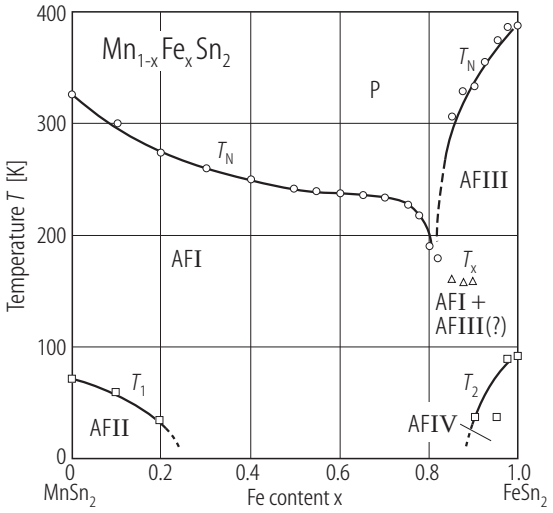

Fig. 67. $Mn_{1-x}Fe_xSn_2$. Magnetic phase diagram in composition - temperature plane [93S4]. P: paramagnetic; AF: antiferromagnetic. I to IV label the magnetic-structure types. In the first two, the atomic moments align parallel within each of (110) planes, which, in turn, are arranged as + – + – in type I but as + + – – in type II. Types III and IV are those shown in Fig. 107 (a) and (b), respectively.

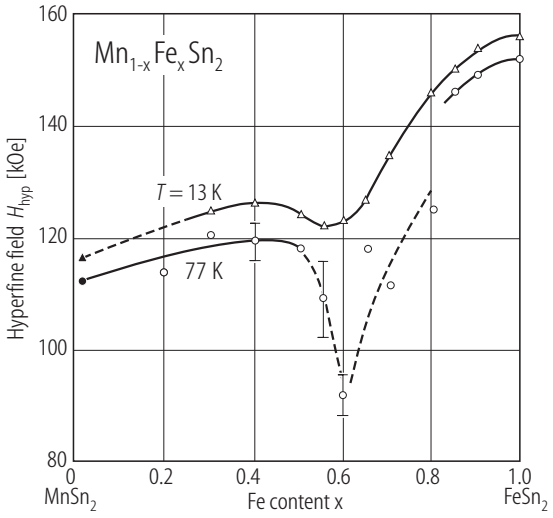

Fig. 68. $Mn_{1-x}Fe_xSn_2$. Hyperfine field H_{hyp} at ^{57}Fe at 13 K and 77 K plotted against the composition parameter x. Solid symbols show the values obtained by [82L1] at 86 K and 4.2 K, respectively [93S2, 93S4].

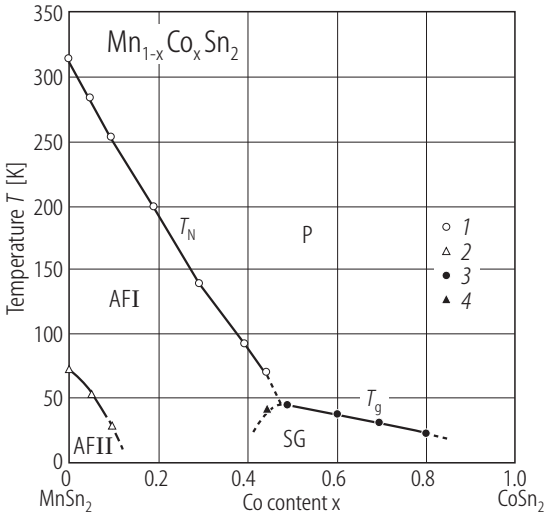

Fig. 69. $Mn_{1-x}Co_xSn_2$. Magnetic phase diagram in a composition - temperature plane. The data were obtained from dc (*1*, *2*) and ac (*3*) susceptibility measurements. The temperature below which the field cooling effect is observed is also plotted (*4*) [90S1]. P: paramagnetic; SG: spin glass; AF: antiferromagnetic. Magnetic structure types I and II are described in the caption of Fig. 67.

1.5.4.5 Fe alloys and compounds

1.5.4.5.1 Alloys and compounds with C and Si

The $Fe_{3-x}Mn_xSi$ system has attracted much attention, since in this range Fe_3Si is ferromagnetic, the Heusler alloy Fe_2MnSi has a complex magnetic behaviour, and Mn_3Si is antiferromagnetic.

Survey

	Composition x	Properties	Figure	Table
$(Fe_{0.7}Mn_{0.3})_{1-x}C_x$	0...0.036	$T_N(x)$, $T_{tr}(x)$	70	
$(Fe_{1-x}Ni_x)_{92}C_8$	0...0.4	x-T magnetic phase diagram	71	
$(Fe_{1-x}Si_x)_3Si$	0.06	NMR-ON spectra of ^{60}Co	72	
	0.035	$M^2(Q)$, $\boldsymbol{Q} \parallel [110]$	73	
$Fe_{3-x}Cr_xSi$	0.1...0.4	$p_m(x)$	74	
	0...0.4	$H_{hyp}(x)$	75	
$Fe_{3-x}Mn_xSi$	1.2, 1.5	$\chi_{ac}(T;x)$	76	
	1.70, 1.75	$H_{tr}(T;x)$	77	
	0...0.3	$H_{hyp}(x)$	78	
	0.32	$D(T)$	79	
	0.9...1.5	$\alpha(T;x)$	80	
$Fe_2Mn_{1-x}V_xSi$	0...1	$p_m(x)$, $p_{m,eff}(x)$, $T_C(x)$, $\Theta(x)$	81	
$Fe_{3-x}Co_xSi$	0...1.8	$H_{hyp}(x)$	82	
	0...2	$\Gamma(x)$ of Mössbauer spectrum	83	
	0...2	$K_1(x)$	84	
FeSi		$I_{ND}(T)$, a	85	8
$FeSi_2$		a, b, c		8
$Fe_{1-x}Mn_xSi$	0.2...0.97	$\alpha(T;x)$	86	
$Fe_{1-x}Co_xSi$	0...0.60	$\alpha(T;x)$	86	
	0.1...0.7	$\sigma(T)$, $\chi_g^{-1}(T)$	87	
	0.1...0.7	$\overline{p}_{at}(x)$, $p_{eff}(x)$	87	
	0.4	spin density map	88	
	0.2	$I_{ND}(H)$	89	
	0.2	$\sigma(H)$, $H_s(\theta)$	90	
	0.2	T-H magnetic phase diagram	91	
	0.2	ESR $\omega(H_r)$	92	

Table 8. Supplement to Table 9 in LB III/19C, subsect. 1.5.4.5.1. Magnetic and related properties of FeSi [88T1] and $FeSi_2$ [71D1].

	FeSi	$FeSi_2$	
		T > 937 °C [90m]	T < 982 °C [90m]
Crystal structure	cubic B20	tetragonal	orthorhombic
		*tP*3, P4/mmm	*oC*48, Cmca
Phase name		ζ_α or α	ζ_β or β

	FeSi	$FeSi_2$	
a [Å]	4.500 [63W]	2.684	9.863
b [Å]			7.791
c [Å]		5.128 [91v]	7.833
Magnetism	temperature-induced para		remanence magnetization of 0.01 G at $T < 100$ K for *p*-type semiconducting compound [94A1].

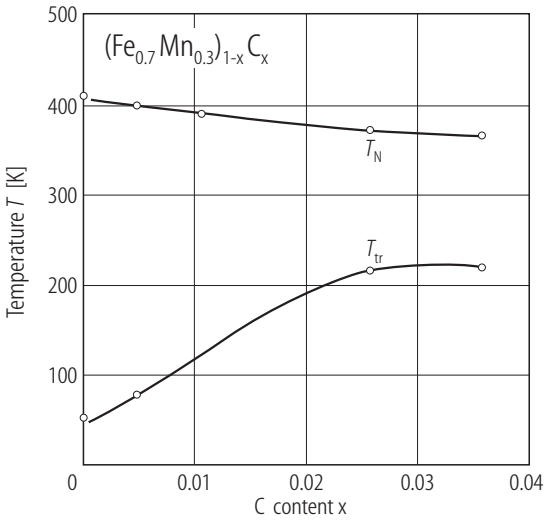

Fig. 70. $(Fe_{0.7}Mn_{0.3})_{1-x}C_x$. Composition dependence of the Néel temperature T_N and another transition temperature T_{tr} below which cooling in a magnetic field of 50 Oe leads to a higher value of the magnetic susceptibility than zero-field cooling, as determined from susceptibility measurements [88S2].

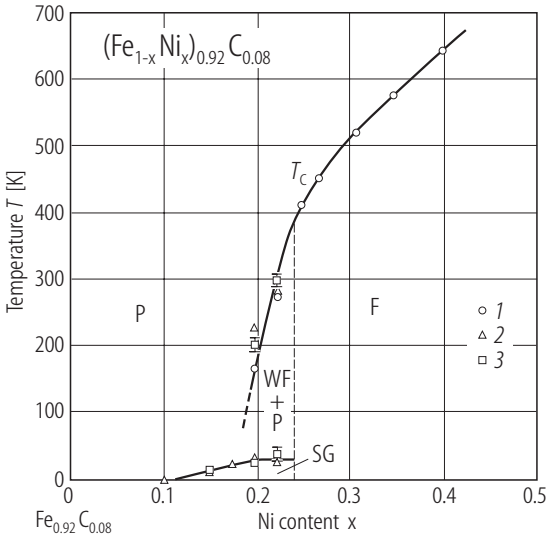

Fig. 71. $(Fe_{1-x}Ni_x)_{0.92}C_{0.08}$. Magnetic phase diagram in a composition - temperature plane of the FCC alloy. P: paramagnet; F: ferromagnet; WF: weak ferromagnet; SG: spin glass. (*1*) Arrott plots; (*2*) ac susceptibility; (*3*) Mössbauer effect [86I2].

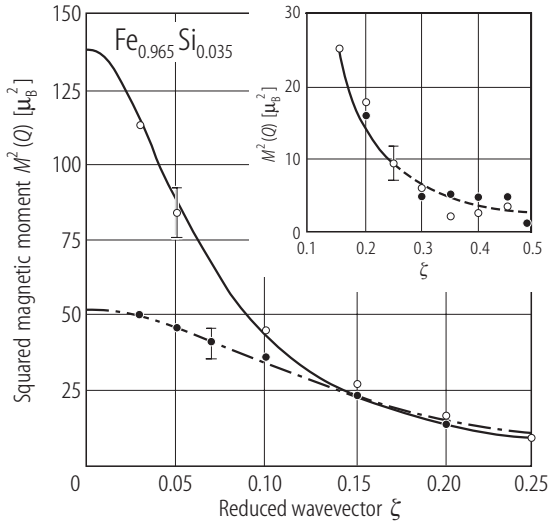

Fig. 73. $Fe_{0.965}Si_{0.035}$. Wave-vector dependence of the integrated paramagnetic-scattering intensity of polarized neutrons. The data at temperatures $1.10T_C$ (open circles) and $1.25T_C$ (solid circles), where T_C = 1032 K is the Curie temperature, at $\boldsymbol{Q} = (2\pi/a)(1+\zeta,1+\zeta,0)$ are plotted against the relative wave vector ζ, after converted into $M^2(Q)$, the Fourier transform of spatial distribution of squared magnetic moment. The phonon scattering at the respective temperatures is used in the calibration. The reciprocal lattice vector $d^*(110) = 3.07$ Å^{-1} at T_C. The curves are the fits to the Lorentzian expression of $M^2(Q)$. The inset shows the same plots up to the Brillouin zone boundary [86S2].

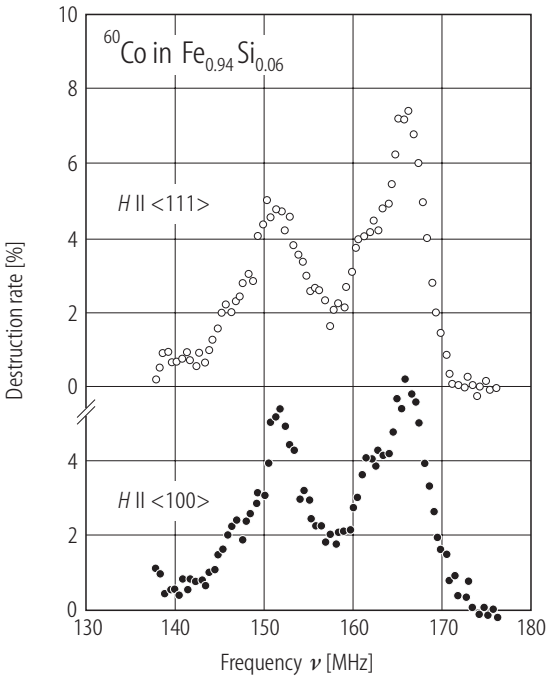

Fig. 72. $Fe_{0.94}Si_{0.06}$. NMR spectra of ^{60}Co doped in the alloy. Resonance intensities detected through NMR-ON (oriented nuclei) technique as the destruction rate (%) of the nuclear orientation are plotted against the rf frequency. Measurements were carried out at about 0.009 K, with a frequency modulation of ± 0.5 MHz in a magnetic field of 2 kOe along <111> and <100> directions [90O2].

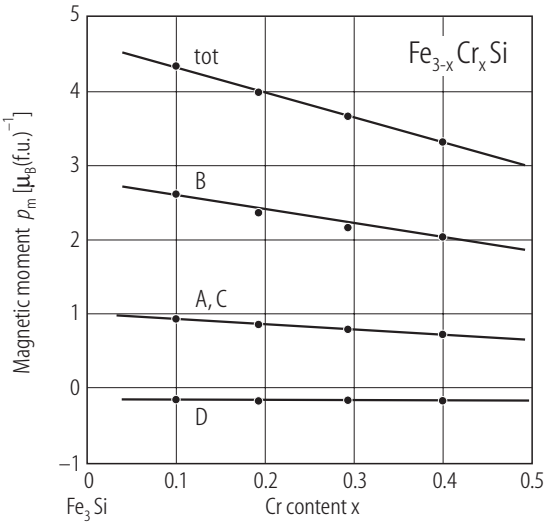

Fig. 74. $Fe_{3-x}Cr_xSi$. Dependence of the magnetic moment per formula unit, p_m, at room temperature on Cr concentration x. tot: total magnetic moment; B, A, C, D: magnetic moments of the respective sublattices. The total moment is the spontaneous magnetic moment determined through extrapolation from magnetic measurements, while the sublattice magnetic moments are determined from neutron powder diffraction [94W1]. See 1.5.4.1 Introduction for the sublattices of $D0_3$ type of crystal structure of this compound.

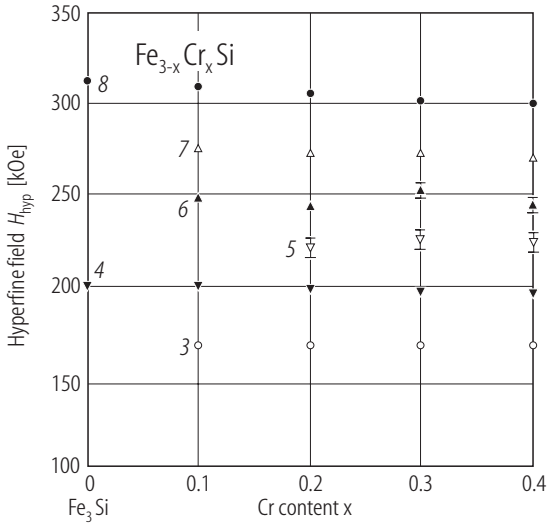

Fig. 75. $Fe_{3-x}Cr_xSi$. Dependence of hyperfine fields H_{hyp} at the ^{57}Fe atoms on the Cr concentration. The fields were derived from Mössbauer spectra at room temperature. The numerals in the figure refer to the number of nearest-neighbour Fe atoms [93S1].

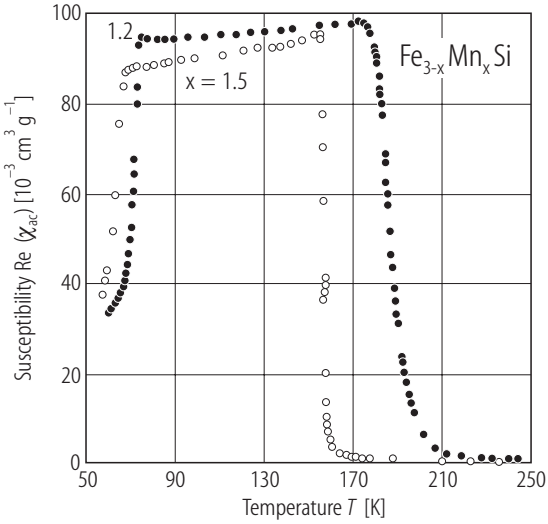

Fig. 76. $Fe_{3-x}Mn_xSi$. x = 1.2, 1.5. Temperature dependence of the real part of the ac susceptibility. The data were taken in an rms magnetic field of about 4 Oe with frequency 433 Hz [91C2].

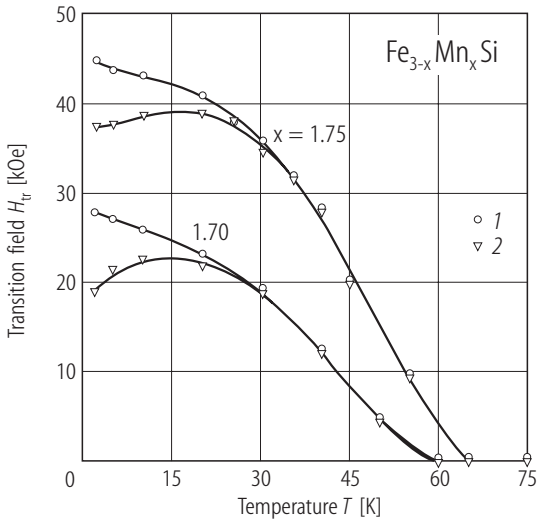

Fig. 77. $Fe_{3-x}Mn_xSi$. x = 1.75, 1.70. Temperature dependence of the magnetic field H_{tr} at which a transition between spin-glass-like to an apparently ferromagnetic state takes place. (*1*) increasing applied field; (*2*) decreasing applied field [93A1].

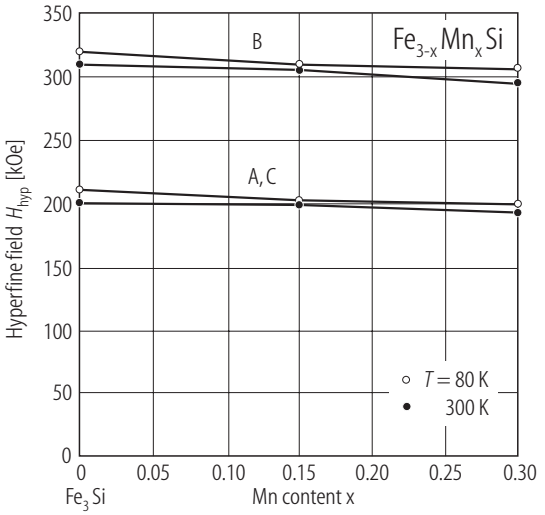

Fig. 78. $Fe_{3-x}Mn_xSi$. Dependence of the average hyperfine fields H_{hyp} at ^{57}Fe atoms on the Mn concentration, as derived from Mössbauer spectra at 80 K and 300 K. The higher fields correspond to B sublattice sites and the lower fields to A, C sublattice sites [89K1]. See 1.5.4.1 Introduction for sublattices.

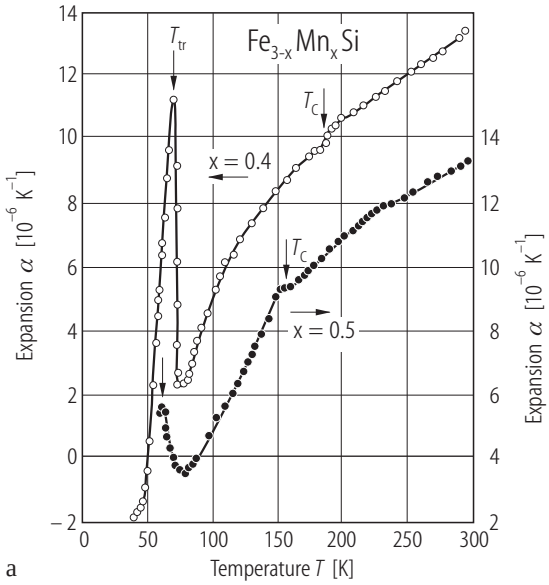

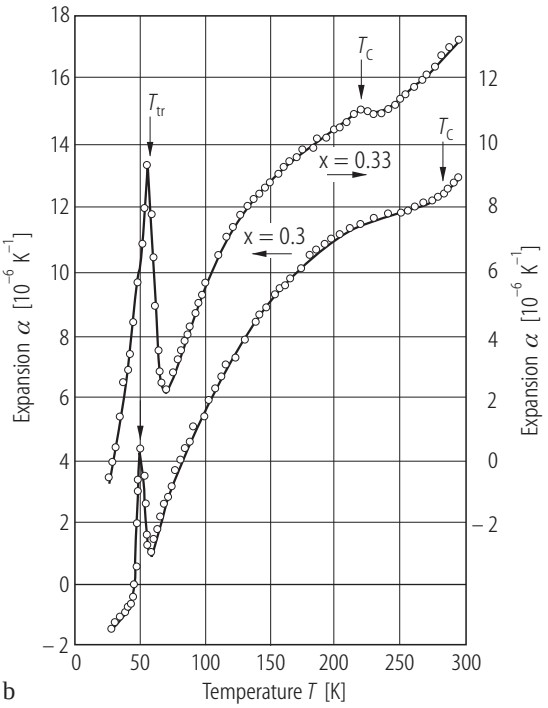

Fig. 80. $Fe_{3-x}Mn_xSi$. Temperature dependence of the thermal expansion coefficient α for (**a**) x = 0.4, 0.5 and (**b**) x = 0.3, 0.33 [92L1].

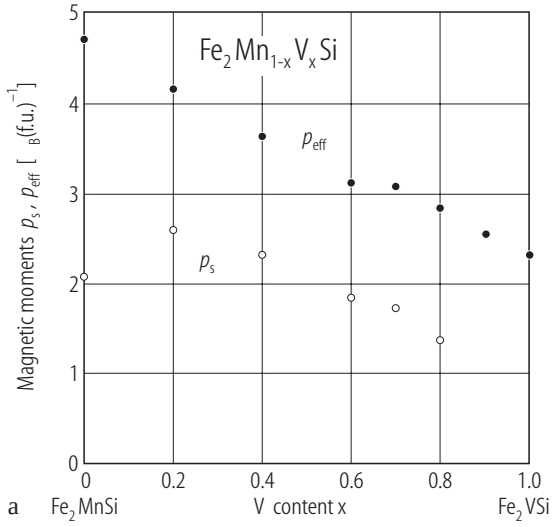

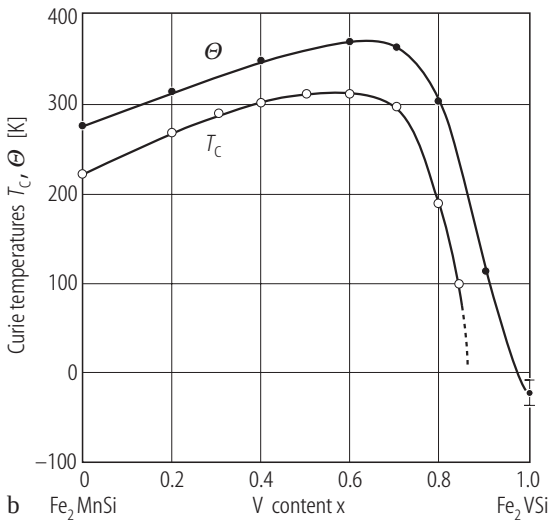

Fig. 81. $Fe_2Mn_{1-x}V_xSi$. Composition dependence of (**a**) the saturation and effective magnetic moments per formula unit, p_s and p_{eff}, and (**b**) the ferromagnetic and paramagnetic Curie temperatures, T_C and Θ [93K3].

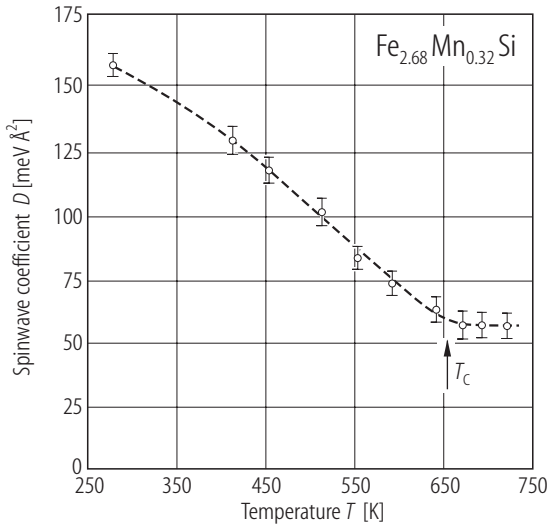

Fig. 79. $Fe_{2.68}Mn_{0.32}Si$. Temperature dependence of the spin-wave stiffness constant D [86K2].

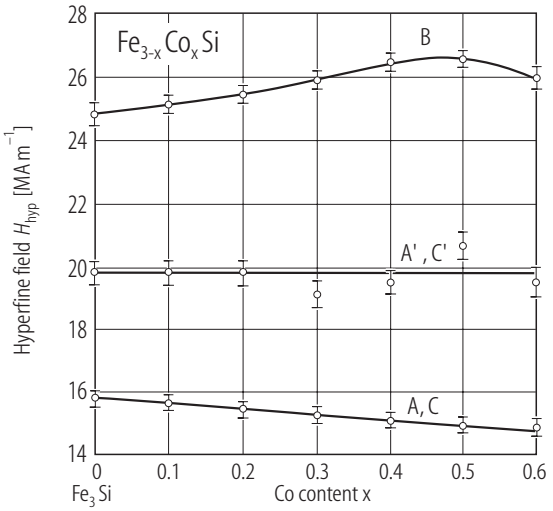

Fig. 82. $Fe_{3-x}Co_xSi$. Dependence of the hyperfine fields H_{hyp} at ^{57}Fe atoms at various sublattice sites on the Co concentration, as derived from Mössbauer spectra at room temperature [85D1]. See 1.5.4.1 Introduction for the definition of the sublattices. A' and C' denote A and C sites, respectively, with 5 nearest neighbour Fe atoms. 1 MA $m^{-1} = 4\pi$ kOe.

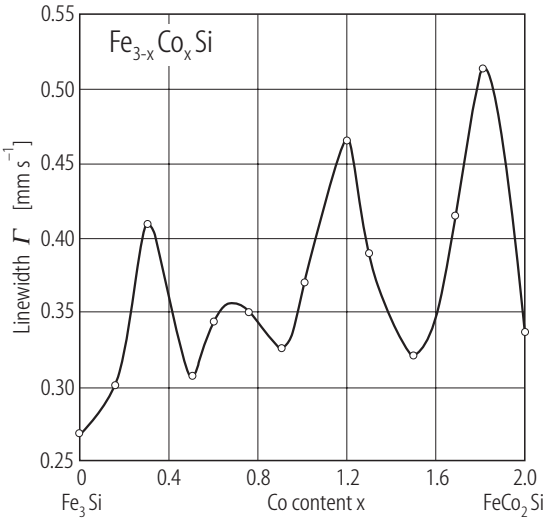

Fig. 83. $Fe_{3-x}Co_xSi$. Dependence of the halfwidth Γ of the outermost lines of the Mössbauer spectra, at room temperature, on Co concentration [86K1].

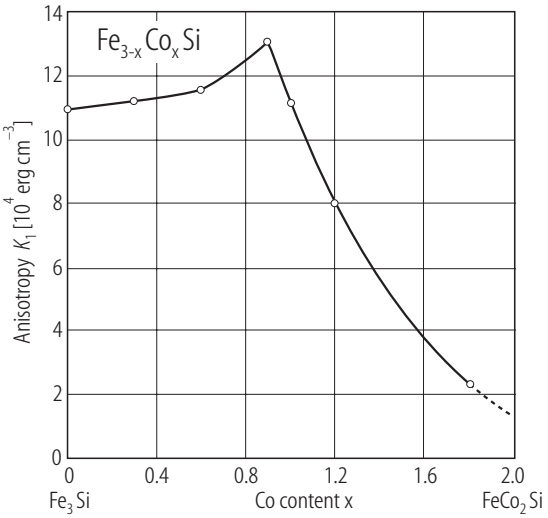

Fig. 84. $Fe_{3-x}Co_xSi$. Dependence of magnetocrystalline anisotropy constant K, extrapolated to 0 K on Co concentration [86K1].

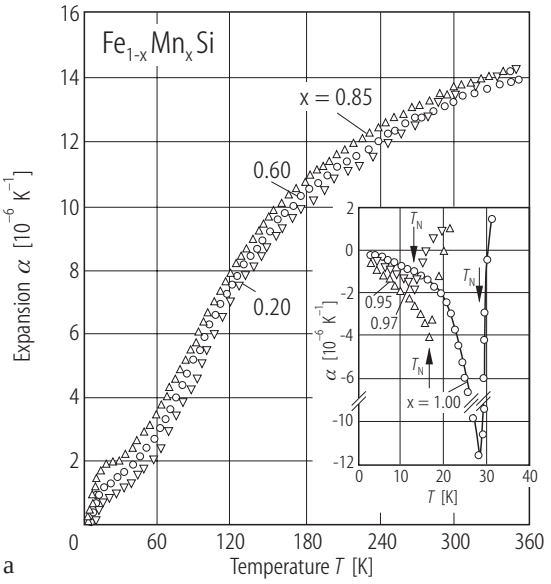

a

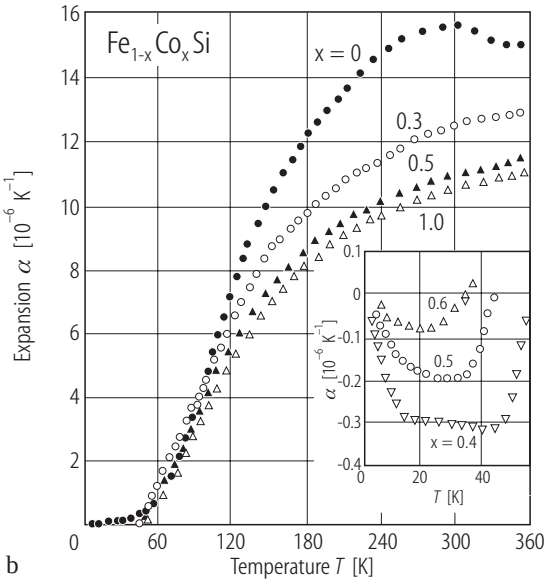

b

Fig. 86. $Fe_{1-x}Mn_xSi$ (**a**) and $Fe_{1-x}Co_xSi$ (**b**). Temperature dependence of the linear thermal expansion coefficient α [89P1].

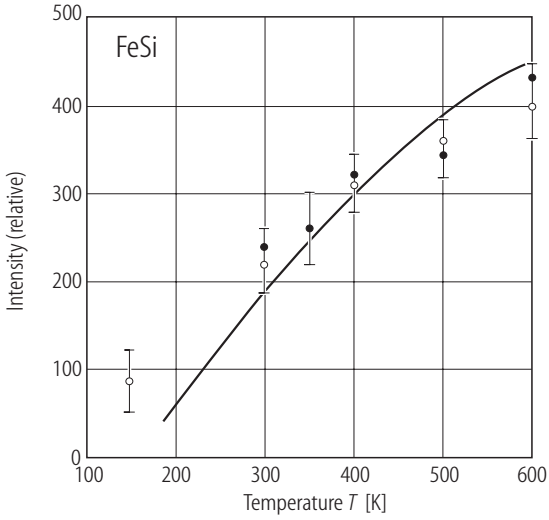

Fig. 85. FeSi. Temperature dependence of the integrated line intensity in a polarized-neutron magnetic scattering experiment. The intensity data (open circles) were obtained from constant-q spectra at $(1+\zeta, 1+\zeta, 0)$ and found to be independent of ζ. Solid circles: M^2 determined from Lorentzian fitting of the spectra [88T1]; solid line: $3k_B T\chi$ from static magnetic susceptibility data by [67J1].

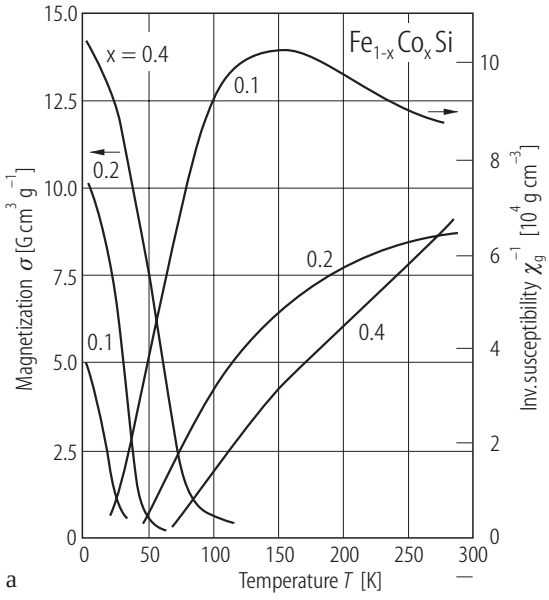

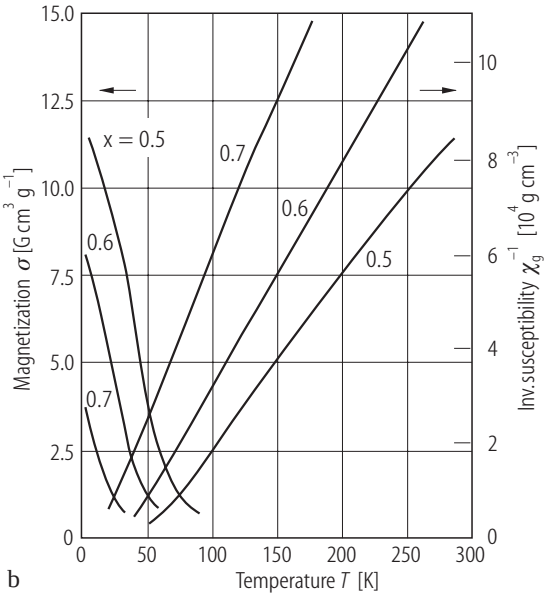

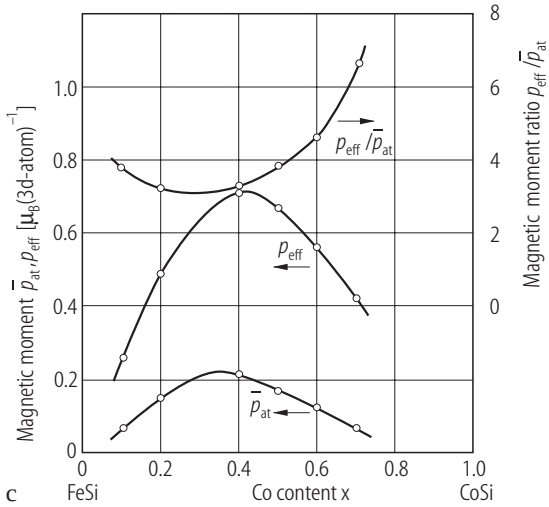

Fig. 87. $Fe_{1-x}Co_xSi$. (**a**, **b**) Temperature dependence of the mass magnetization σ and of the inverse magnetic mass susceptibility χ_g^{-1} for various compositions, as measured in a magnetic field of 10 kOe applied parallel to the [001] axis [92I1]. (**c**) Dependences on Co concentration of ferromagnetic moment $\bar{p}_{at}$, the paramagnetic moment per magnetic atom, p_{eff}, and their ratio $p_{eff} / \bar{p}_{at}$ [92I1].

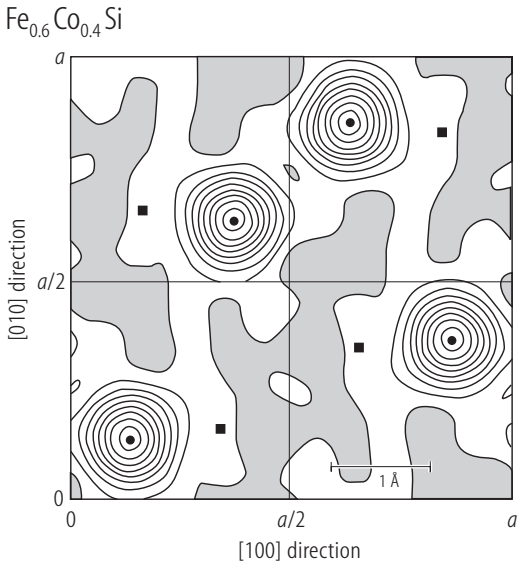

Fig. 88. $Fe_{0.6}Co_{0.4}Si$. Projection of the magnetic moment density to the (001) plane at 4.2 K in a magnetic field of 9.7 kOe perpendicular to the plane. The contours are in units of 0.05 $\mu_B/Å^2$. The moment is negative in the hatched regions. Solid circles : Fe, Co site; solid squares: Si site [92I1].

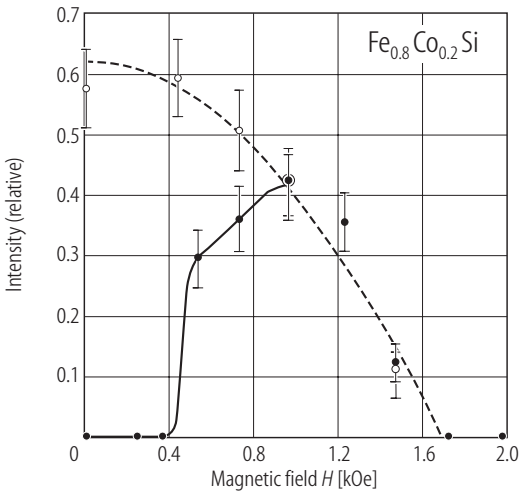

Fig. 89. $Fe_{0.8}Co_{0.2}Si$. Magnetic-field dependence of the integrated intensity of a polarized-neutron magnetic diffraction line at 23 K. The crystal has initially its helical spin structure along the [111] direction; the magnetic field was applied along the $[11\bar{1}]$ direction. The intensity was measured on a satellite line of (000) in the field direction. Solid circles: increasing applied magnetic field; open circles: decreasing fields [86I1].

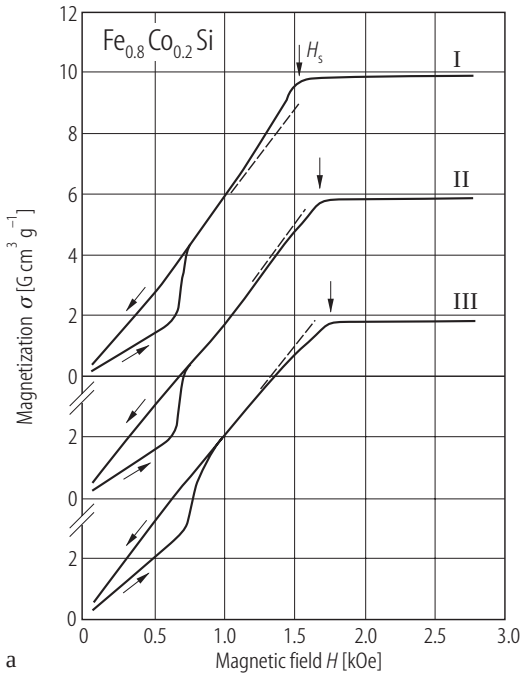

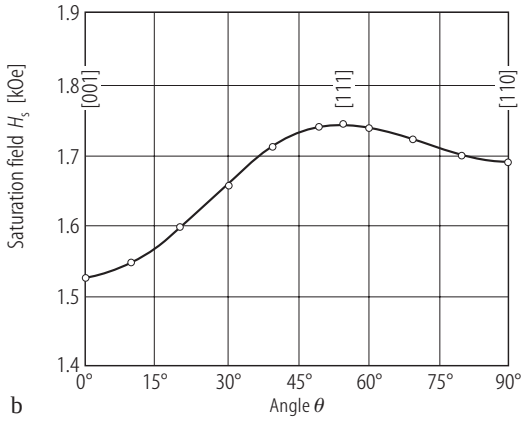

Fig. 90. $Fe_{0.8}Co_{0.2}Si$. (**a**) Dependence of mass magnetization σ on applied magnetic field H at 4.2 K [93I1]. The specimen was premagnetized in a field H_0 = 3.0 kOe along one direction and followed by a decrease of this field to zero. The magnetization curve was then measured in a field H along another direction. H_s: saturation field. I: $H_0 \parallel [110]$, $H \parallel [001]$; II: $H_0 \parallel [001]$, $H \parallel [110]$; III: $H_0 \parallel [001]$, $H \parallel [111]$. (**b**) Dependence of saturation field H_s, at 4.2 K on the crystallographic direction [93I1].

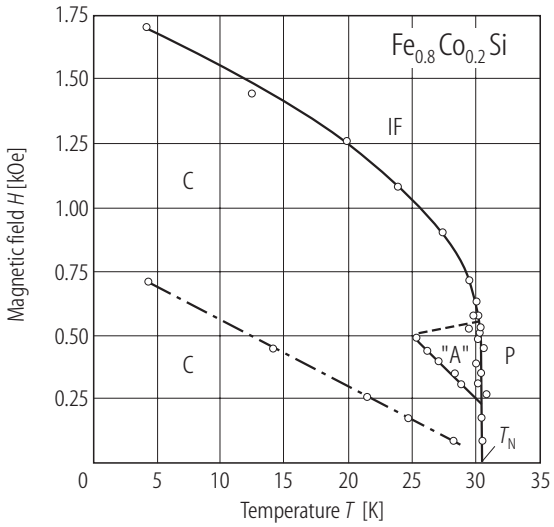

Fig. 91. $Fe_{0.8}Co_{0.2}Si$. Magnetic phase diagram in a magnetic field vs. temperature plane, as determined from magnetic measurements on a single crystal with the magnetic field H along the [110] direction. The compound has a helical spin structure for H = 0. C: conical arrangement of the spins; IF: field-induced ferromagnetism; P: paramagnetism; "A": unknown spin structure with a dip of magnetization. The chain line within the C region indicates a reorientation of the propagation vector of the cone-type magnetic structure to the direction of the applied magnetic field, when it is not along the field initially [90I1].

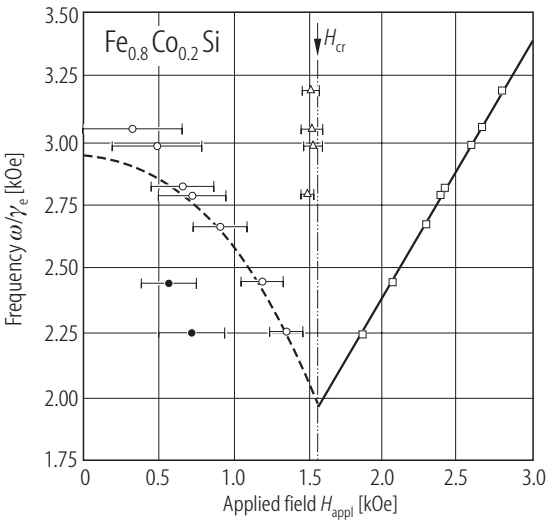

Fig. 92. $Fe_{0.8}Co_{0.2}Si$. ESR frequency ω/γ_e at 4.2 K plotted against the magnetic field applied, H_{appl}, along the [001] axis of a single crystal. H_{cr} is the critical field for induced ferromagnetic spin structure. The broken curve shows the theoretical curve for a helical spin resonance based on the antisymmetric exchange interaction of the Dzyaloshinski-Moriya type. The frequency is expressed in terms of ω/γ_e, the angular frequency divided by the magnetomechanical ratio of a free electron [89W1].

1.5.4.5.2 Alloys and compounds with Ge

The existence of two successive magnetic transitions in $FeGe_2$ has been established by [85C1] and the proposed collinear spin structure at lower temperature range seems to be supported theoretically [91G1], but it is still the subject of active discussion, because neither the anisotropy of magnetic susceptibility nor the magnetization curves in strong magnetic fields are consistent with the collinear spin structure [89Z1]. For the related ternary compound $Fe_{1-x}Co_xGe$ it is claimed [88P1] that crystal defects increase in the single-crystal specimens as x increases. This may lead to another complication for the physical properties of these compounds.

In the series of ternary compounds $Fe_{3-x}V_xGe$, doubly ordered cubic, $L2_1$ (Heusler alloy) type of crystal structure has been established through pulsed neutron powder diffraction at room temperature for x = 0.6, 0.8 and 1.0. The latter compound contains a small amount of undetermined second phase [90B1].

Survey

	Composition x	Properties	Figure	Table
$\alpha Fe_{1-x}Ge_x$	0.004...0.04	H_{hyp}(x) at ^{69}Ge	93	
$\gamma(Fe_{0.7}Mn_{0.3})_{1-x}Ge_x$	0...0.087	$\chi(T;x)$, T_N(x)	94, 95	
Fe_3Ge		a, c, H_{hyp}, ΔE_Q, IS		9